Modeling of Tsunami Detection by High Frequency Radar Based on Simulated Tsunami Case Studies in the Mediterranean Sea

Stéphan T. Grilli[1], Samuel Grosdidier[2] and Charles-Antoine Guérin[3]
(1) Department of Ocean Engineering, University of Rhode Island, Narragansett, RI, USA
(2) Diginext Ltd., Toulouse, France
(3) Université de Toulon, CNRS, Aix Marseille Université, IRD MIO UM 110, La Garde, France

ABSTRACT

Where coastal tsunami hazard is governed by near-field sources, such as Submarine Mass Failures (SMFs) or meteo-tsunamis, tsunami propagation times may be too small for a detection based on deep or shallow water buoys. To offer sufficient warning time, it has been proposed to implement early warning systems relying on High Frequency (HF) radar remote sensing, that can provide a dense spatial coverage as far offshore as 200-300 km (e.g., for Diginext's Stradivarius radar). Shore-based HF radars have been used to measure nearshore currents (e.g., CODAR SeaSonde® system (http://www.codar.com/), by inverting the Doppler spectral shifts, these cause on ocean waves at the Bragg frequency. Both modeling work and an analysis of radar data following the Tohoku 2011 tsunami, have shown that such radars could be used to detect tsunami-induced currents and issue tsunami warning. However, long wave physics is such that tsunami currents will only raise above noise and background currents (i.e., be at least 10-15 cm/s), and become detectable, in fairly shallow water, which would limit direct HF radar detection to nearshore areas, unless there is a very wide shelf.

Here, we use numerical simulations of both tsunami propagation (in the Mediterranean basin) and HF radar remote sensing to develop and validate a new type of tsunami detection algorithm that does not have these limitations. This algorithm computes correlations of HF radar signals at two distant locations, shifted in time by the tsunami propagation time computed between these locations (easily obtained based on bathymetry). We show that this method allows detection of tsunami currents as low as 5 cm/s, i.e., in deeper water, beyond the shelf and further away from the coast, thus providing an earlier warning of tsunami arrival.

INTRODUCTION

In the past decade, two major tsunamis, the 2004 Indian Ocean (IO) tsunami (Grilli et al., 2007; Ioualalen et al., 2007) and the 2011 Tohoku tsunami (Grilli et al., 2013), caused tens of thousands of fatalities and enormous destruction in Indonesia (and 6 other countries in the IO basin) and in Japan. These two extreme events, which were triggered by the 3rd and 5th largest earthquakes ever recorded, $M_w = 9.3$ and 9.1, respectively, reminded us that tsunamis are among the most devastating natural disasters that can impact our increasingly populated coastal ar-

eas. Besides their enormous destructive power, the hazard posed by large tsunamis can be reinforced when their source is located close to the nearest coastal areas, and thus both their energy spreading is low and their propagation time is short. In the latter case, warning times will also be short, particularly using traditional means of detection such as seafloor pressure sensors or buoys, and thus there will be little time for completely evacuating coastal populations. Moreover, standard point data measurements of incoming tsunami waves (i.e, pressure gages or buoys) are local and, hence, may not record the incoming tsunami waves if they are also localized, and are often destroyed by the earthquake or the tsunami in the most impacted areas. A short tsunami propagation time was one of the reasons for the high casualties in Banda Aceh, Indonesia, during the 2004 IO tsunami, which was impacted by large waves and inundation only 15-20 min after the earthquake was triggered in the nearby Sumatra-Andaman subduction zone. Likewise, during the 2011 Tohoku tsunami, large waves and inundation arrived in northern Honshu only 20-25 min after the earthquake triggering in the nearby Japan Trench (JT), causing the nearly complete destruction of some coastal cities and killing entire populations who had been unable to evacuate, despite the dire warnings that they eventually received, that the earthquake and tsunami were much larger than initially estimated.

While such extreme seismic events are fortunately quite rare, in coastal regions of the world with moderate seismicity, the greatest tsunami risk from near-field sources may result not from co-seismic tsunamis, but from tsunamis induced by submarine mass failures (SMFs) or from meteotsunamis. SMFs can be triggered on or near the continental shelf break or slope, by earthquakes as low as $M_w = 7$, that are much more frequent than megathrust earthquakes; given enough sediment accumulation, huge volumes of sediment can be mobilized over significant vertical drops and generate very large "landslide" tsunamis (Grilli and Watts, 2005). Meteotsunamis are tsunami-like long waves generated by unusual weather systems, causing fast moving squalls with low atmospheric pressure. If these systems move at or close to the long wave celerity on the shelf, much of their energy can be transferred to waves by way of resonance In June 2013, a meteotsunami was triggered along the US upper east coast, which caused significant resonant oscillations in many harbors in the region, particularly in Rhode Island; this meteotsunami was recorded as far as Puerto Rico.

Although few confirmed landslide tsunamis have been identified in recent history, they have been devastating. The 1998 Papua New Guinea tsunami is one such case, where a $M_w = 7.1$ earthquake only caused a moderate tsunami, but then triggered, with some delay, a large and deep underwater slump (i.e., a nearly rigid rotational SMF), which caused much more devastating waves that killed over 2,000 people on the nearby Sissano spit (Tappin et al., 2008). Large SMFs can also be associated with large earthquakes. After observing, through careful modeling of the seismic source and resulting co-seismic tsunami, that they could not reproduce the up to 40 m inundation and runup that destroyed the Sanriku area during the 2011 Tohoku tsunami, many scientists concluded that there should have been some other source or mechanism at play to explain the tsunami generation, such as splay faults or SMFs (Grilli et al., 2013). Based on analyses of wave and seafloor data, Tappin et al. (2014) identified and parameterized a large post-earthquake 500 km³ SMF, deep near the JT, north of the main rupture, whose motion could have generated additional higher-frequency waves similar to those observed at several nearshore buoys. A detailed modeling of wave generation and propagation from a dual seismic-SMF source closely reproduced all the observations made at nearshore and deep water buoys, and runup and inundation measured onshore.
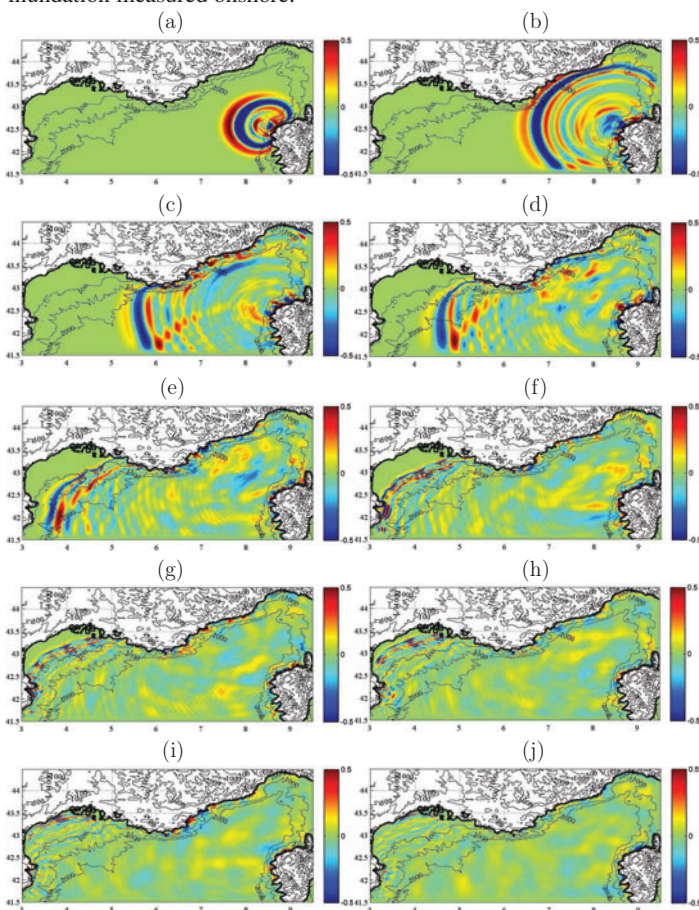

Fig. 1: Numerical modeling of a landslide tsunami generated by a SMF in West Corsica (SE corner area), to the Golf of Lion (NW area). Color scale is surface elevation and black contours are bathymetry in meter. Panels show snapshots of simulations with the long-wave propagation model FUNWAVE-TVD, after: (a) 10'; (b) 20'; (c) 30'; (d) 40'; (e) 50'; (f) 1h; (g) 1h10'; (h) 1h20'; (i) 1h30'; and (j) 1h40' of propagation, initialized at 425 s with results of tsunami generation model NHWAVE.

Because they need large sediment accumulation to occur, SMFs are triggered more often on continental slopes, in underwater canyons offshore of large estuaries, or on the steeper parts of accretionary prisms onshore of major subduction zones. Potentially large landslide tsunamis can be generated from such near-field sources, for which there will be short propagation and warning times. To assess SMF tsunami hazard along the upper US East Coast, Grilli et al. (2009) conducted a probabilistic analysis based on Monte Carlo simulations (MCS) of slope stability and tsunami generation. MCS results reproduced well the statistical distributions of areas, volumes, and types (slide or slump) of SMFs found in marine geology surveys, and identified regions of elevated SMF tsunami hazard, in terms of 100 and 500 year return period runup. These were mostly north of the Carolinas with, as expected, elevated risk off of some major estuaries such as the Hudson River and Chesapeake Bay. The largest known historical SMF in the region, the Currituck slide complex, which is over 25,000 years old and 165 km³ in volume, is in fact located offshore of the latter. Tsunami generation from this large SMF was modeled by Grilli et al. (2015), who showed that if it occurred nowadays, the tsunami would flood heavily populated coastal areas of Virginia, Maryland, New Jersey and the Chesapeake Bay, with up to 5 m inundation, after 1h to 2h of propagation depending on distance to the source (travel time in this particular case is not that short, due to the very wide shelf in the area, but the SMF and tsunami occurrence might not easily be detected by standard instruments).

Tsunami warning centers have been in operation in the US for over 40 years, in Hawaii (PTWC) and Alaska (NTWC), essentially to cover sources in the Pacific Ocean. Over the years, both centers have been issuing rapid and reliable warnings, together with specific tsunami runup/inundation forecasts for many far-field locations, whenever a significant earthquake occurred in their geographic area. Regarding landslide tsunamis, however, the centers have only been issuing warnings when some seismic threshold was reached in previously identified regions, that near-field landslide tsunamis were possible. It is only when tsunamis are measured (usually after they have propagated to the location of deep water buoys) that the centers can confirm that there was actual tsunami generation, which may take up to 1h. Thus, in situations described above with near-shore seismic or SMF sources, there may not be enough time with current realtime sensing systems to issue a warning that is based on actual tsunami data. For non-seismically induced nearshore SMF tsunamis or for meteotsunami events, there may not even be enough time to issue a first warning.

TSUNAMI DETECTION BY HF RADAR

Detection of currents by HF radar

In this work, we show that shore-based High Frequency (HF) radars can be used to provide early warning for tsunamis generated nearshore, given proper detection algorithms. In recent years, HF radar remote sensing of coastal currents has been operational, in particular, in US coastal waters, based on the CODAR SeaSonde® system (http://www.codar.com/) With this technology, currents are detected by measuring the Doppler shift they induce on the radar signal. The principle of using HF radar for tsunami warning was proposed almost 40 years ago by Barrick (1979) and, more recently, was supported by numerical simulations Lipa et al. (2006). These authors showed that a catastrophic tsunami such as the 2004 IO tsunami could have been detected at some distance offshore if HF radars had been installed in Indonesia. Other numerical studies based on an alternative HF radar system, the WERA system (http://www.helzel.com/de/6035-wera-remote-ocean-sensing), have reached similar conclusions (Heron et al., 2008; Dzvonkovskaya et al., 2009; Gurgel et al., 2011). Direct measurements of the recent and similarly extreme 2011 Tohoku tsunami were made by shore-based HF radars, in the near-field in Japan (Hinata et al., 2011; Lipa et al., 2011, 2012) and in the far-field in Chile (Dzvonkovskaya, 2012). No realtime

tsunami detection algorithms were in place, but an *a posteriori* analysis of the radar data identified the tsunami current in the measurements. In these earlier studies, simple tsunami detection and warning algorithms were proposed, based on the magnitude of the tsunami current inferred from the radar Doppler spectrum. As we shall see, however, for this approach to work, the tsunami current must be sufficiently strong to raise above background noise and currents, which depending on the area could be as high as 0.10 m/s. Hence, the tsunami current must be at least $U_t \sim 0.10 - 0.15$ m/s for this method to work (this will be illustrated later in the paper), which limits direct detection to fairly shallow water and thus nearshore locations; this also means short warning times, unless there is a very wide shelf.

Here, we propose a new tsunami detection algorithm, based on HF Radar measurements, that does not have this limitation and could thus be implemented as part of a tsunami early warning system. We develop and validate this new algorithm by way of numerical simulations of both tsunami and radar signal, using simulated tsunami wave trains. We illustrate our method using the characteristics of a new type of HF radar, referred to as Stradivarius, that is being developed by Diginext Ltd and was deployed in southern France in late 2014, to cover the Golf of Lion along the Mediterranean coast (Figs. 1, 2). This radar has a lower carrier electromagnetic wave (EMW) frequency $f_{EM} = 4.5$ MHz, than currently deployed HF radars for measuring coastal currents, and EMW propagation mode within the atmosphere-ocean interface that allows to remotely sense beyond the horizon. In a bistatic configuration and using efficient antennas and wave forms, Stradivarius has been shown in field experiments to measure currents up to 200-300 km distances, depending on the radar power and environmental noise.
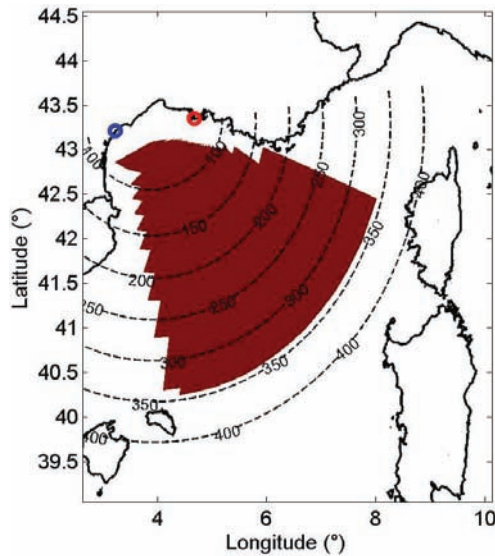

Fig. 2: Stradivarius radar deployment in Golf of Lion, Mediterranean sea (Fig. 1): (solid brown) area of coverage, (blue symbol) transmitter location, (red symbol) indicates the receiver location, and (dashed lines) equivalent monostatic distance from radar in km.

It should be stressed that the main goal of this preliminary study is to demonstrate the validity of the new detection algorithm for an idealized framework, using purely simulated data. The radar will be assumed to work in a monostatic configuration (which is the limiting case of Stradivarius' actual bistatic configuration, for long ranges), with a direction of observation perpendicular to the coast. Both the bathymetry and the tsunami wave train will be assumed to be invariant along the coast, so that tsunami wave crests will approach the coast perpendicular to the radar line-of-sight; this is in fact a fairly good approximation for many

cases of tsunami propagation over a wide shelf (e.g., Fig. 1). More realistic configurations will be addressed in forthcoming studies. However, to simulate realistic environmental noise levels, which is important for the validation, the characteristics and performance in field tests of the Stadivarius system will be used in the modeling.

As for all HF radars, the near-surface ocean current is inferred from EMW interactions with ocean surface waves, based on the property that the diffracted radar signal is maximum (i.e., resonates) when it interacts with ocean waves whose wavelength,

$$L_B = \frac{\lambda_{EM}}{2} = \frac{gT_B^2}{2\pi} \quad \text{with} \quad \lambda_{EM} = \frac{c_{EM}}{f_{EM}}, \tag{1}$$

where λ_{EM} denotes the EMW wavelength, $c_{EM} = 299,700$ km/s is the speed of light in the air, and the Bragg frequency $f_B = 2f_{EM}$. For Stradivarius, based on Eq. (1), we find $L_B \simeq 33.3$ m; assuming deep ocean waves the first Eq. (1) further yields the wave period, $T_B = 4.62$ s (with $g = 9.81$ m/s^2, the gravitational acceleration). Wind waves of this period are present in the ocean for wind speeds exceeding about 6 m/s. The lower radar frequency of Stradivarius, therefore, prevents it from measuring currents in calm sea conditions; however, with its large range, the radar is likely to find many regions of the sea with proper wave coverage.

The presence of a tsunami current of magnitude $\pm U_t$ parallel to the main direction of ocean wave propagation will induce a Doppler effect on these, causing a small shift of the Bragg frequency in the radar signal Doppler spectrum, proportional to $\pm U_t$. Computing this shift by processing radar data thus allows estimating the current magnitude $\overline{\tilde{U}_t}(\boldsymbol{x},t)$, averaged (overbar) over a radar cell of dimension Δr in the radial direction and aperture $\Delta\phi_r$ in the azimuthal direction, for a monostatic configuration, centered at $\boldsymbol{x} = (x,y)$, and a measuring (or integration) time interval T_i (tilde). The radar cell spatial dimensions must be sufficiently large to include a statistically meaningful sample of ocean surface waves of various wavelengths (i.e., Δr is a few kilometers). Additionally, as the frequency resolution of the Doppler spectrum near its peak is $\Delta f_D = 1/T_i$, to accurately infer surface currents based on a Doppler shift, the measuring time interval must be sufficiently long, typically 5-10 min for a 12 MHz, but as short as 2 min for a 4.5 MHz, radar frequency. However, the oscillatory nature, in space and time, of an incoming tsunami wavetrain (and of the surface current it induces) means that the larger T_i the lower the maximum value of the estimated current over a given radar cell, due to time averaging of the tsunami signal. Hence, these conflicting requirements must be carefully weighted when selecting parameters of the radar signal processing algorithm; in particular, one can reduce T_i and compensate the loss of resolution this causes by applying a cell-averaging in the radar azimuthal direction on either side of a given radar cell.

Relevant tsunami wave physics
Except for very close to shore, tsunami wave trains can be accurately represented by linear long wave theory (Dean and Dalrymple, 1984), as their characteristic wavelength is large compared to depth, $L_t \geq 20\,h$ with $h(x,y)$ the local depth, and they have a very small steepness. This means, tsunami-induced horizontal currents, $\boldsymbol{U}_t$, can be assumed nearly uniform over depth and thus only function of the horizontal location (x,y) and time t. Also, while phase speed is very large in deep water: $c_t = \sqrt{gh}$, particle velocities, i.e., the induced current, are very small and given by,

$$\boldsymbol{U}_t = \eta_t \sqrt{\frac{g}{h}} \frac{\boldsymbol{k_t}}{k_t} \quad ; \quad \eta_t(x,y) = \eta_{t0} \left\{ \frac{c_{t0}(h_0)}{c_t(h)} \right\}^{\frac{1}{2}} = \eta_{t0} \left\{ \frac{h_0}{h(x,y)} \right\}^{\frac{1}{4}} \tag{2}$$

where η_t is the local tsunami elevation ($\ll h(x,y)$ in deep water), $k_t(x,y,t) = |\boldsymbol{k_t}| = 2\pi/L_t$ the tsunami wavenumber, and $\boldsymbol{k_t} = k_t(\cos\phi_t, \sin\phi_t)$ the wavenumber vector, with ϕ_t the local angle of the tsunami wave ray with respect to the x axis (here typically orientated

shoreward). [The unit vector at the end of Eq. (2) thus points in the local direction of tsunami propagation, $\phi_t(x,y)$]. According to Eq. (2), for linear long waves, the local tsunami elevation η_t can be predicted based on the initial deep water tsunami elevation η_{t0} using Green's law, where $c_{t0} = \sqrt{gh_0}$ is the tsunami initial phase speed in reference depth h_0. Furthermore, long waves refract as a function of depth, even in very deep water, based on changes in phase speed, $c_t(h(x,y))$. Under the geometric optic approximation and for a simple (nearly shore parallel) bathymetry variation (e.g., on the continental shelf), the tsunami direction of propagation $\phi(x,y)$ can be estimated based on Snell's law. However, in general, one must solve as a minimum the "eikonal" equation (Dean and Dalrymple, 1984). Combining refraction with shoaling from Eq. (2), tsunami wave crests will gradually grow in elevation and orient themselves nearly parallel to the local bathymetric contours as they approach shore. Therefore, an incoming tsunami, whatever its initial source location and direction of propagation in a given ocean basin, will eventually arrive in a direction nearly normal to shore and thus propagate essentially straight towards a shore-based radar, with a current magnitude gradually increasing as, $|U_t| = U_t \propto h^{-3/4}$.

According to these fundamental physical properties of tsunami propagation and currents, the tsunami detection algorithm proposed by Lipa et al. (2012), based on "inverting" Doppler spectral shifts, would only be applicable nearshore, over the continental shelf, where tsunami currents would be sufficiently larger than background currents; hence with this method, warning times depend on shelf width and can thus be quite small in some locations. Here, with the Stradivarius radar being able to infer current values as far as 200-300 km, we are proposing and validating a new type of tsunami detection algorithm, based on directly processing the radar signal, which does not require tsunami currents to reach large values to be detectable (e.g., $> 0.10 - 0.15$ m/s). With the new method, the presence of tsunami currents as low as background values, 0.05-0.1 m/s, can be inferred, and thus tsunami detection can occur in deeper water, beyond the continental shelf.

Another advantage of HF radar detection over standard instruments is that it provides a spatially dense set of measurements, over a broad oceanic area, at the scale of the radar cells (e.g., a few km by a few km), in specific local directions. In a monostatic radar configuration, for which the radar transmitter and receiver antennas are collocated, these will be radial directions, while in a bistatic configuration (Fig. 2), where the antennas are separated by a large distance (e.g., tens of km), these will be directions normal to the local ellipse whose focal points are the radar and antenna locations; more details are provided in a following section.

HF RADAR OCEAN SCATTERING MODEL

To simulate tsunami detection by HF radar, we implemented numerical models of both ocean waves and radar backscattering by these, in the presence of a surface current. Upon interacting with a rough, wave-covered, ocean surface of elevation $\eta(r,t)$ (with respect to a position vector $r(x,y)$ defined based on the radar location), EMWs diffract, and a fraction of those EMWs propagates back to the radar receiving antennas, to be measured as the backscattered radar signal $S(t)$. In this process, because the celerity of ocean waves is much less than that of EMWs ($c_B = L_B/T_B \ll c_{EM}$), the ocean surface can be assumed to be stationary. With a linear wave approximation, the radar signal power density spectrum, referred to as "Doppler spectrum" $I(f_D)$ (with f_D the Doppler frequency), has two maxima at the Bragg frequencies $\pm f_B$, for a two-sided spectrum, with each of those corresponding to waves propagating toward or away from the radar, respectively. Nonlinear wave effects, however, cause secondary, lower-energy, peaks to appear in the Doppler spectrum, at frequencies both lower- and higher- than the Bragg frequency.

A surface current $U(r,t)$ causes a shift $\pm \Delta f_B = \pm \tilde{U}(r,t)/L_B$ of the frequencies where the Doppler spectrum is maximum, with respect to

the expected values $\pm f_B$, proportional to the current magnitude, averaged over the radar cell and integration time T_i. Here, the total surface current that affects the radar signal is assumed to be the sum of: (i) a spatially variable, but nearly stationary at the time scale of radar data acquisition ($> \mathcal{O}(T_i)$), residual (mesoscale) current, $U_r(r)$; and (ii) a spatially and temporally varying current, $U_t(r,t)$ induced by the tsunami wavetrain (see, e.g., Eq. (2)); hence, $U(r,t) = U_r(r) + U_t(r,t)$. The residual current, although stationary, is spatially variable in a way that depends on local and synoptic environmental ocean conditions; in a specific case, such a current could be obtained from an operational regional ocean model but, as we shall see, this will not even be necessary to apply the newly proposed tsunami detection algorithm.

Ocean surface model
Assuming a small steepness, the surface elevation of random ocean waves is represented by a second-order perturbation expansion, $\eta(r,t) = \eta_1(r,t) + \eta_2(r,t)$, which is sufficient to accurately simulate both the wave energy density and resulting backscattered HF radar Doppler spectra (Weber and Barrick, 1977; Barrick and Weber, 1977). Accordingly, for the first-order term, we have,

$$\eta_1(r,t) = \frac{1}{\sqrt{2}} \sum_{\varepsilon = \pm} \int \sqrt{\Psi(\pm K)} e^{i(K.r \mp \Omega(K,r,t)t - \varphi^\pm(K))} dK, \qquad (3)$$

where the integration is carried over the wavenumber vector $K = (K_x, K_y) = K(\cos\theta, \sin\theta)$ (with $K = |K|$) and Ψ denotes the directional wave energy density spectrum. The phase $\varphi^\pm(K)$ are random, independent and uniformly distributed between 0 and 2π, and $\pm$ refers to complex conjugates of waves propagating in opposite directions (see below).

The angular frequency of each wave component, $\Omega(K,r,t)$, is modulated by the surface current $U(r,t)$ resulting from both the tsunami wave train and the residual current. Assuming the tsunami current is slowly varying in time at the scale of ocean waves, i.e., the tsunami characteristic period, $T_t \gg T_p$, the peak spectral wave period, we have,

$$\Omega(K,r,t)t = (\Omega_g + K.U_r(r))t + \int_0^t K.U_t(r,\tau)d\tau \qquad (4)$$

where the integral is a memory term representing the cumulative effects of the tsunami current on the instantaneous wave angular frequency, and,

$$\Omega_g = \sqrt{gK\tanh Kh} \qquad (5)$$

is the standard angular frequency of linear gravity waves in depth h (Dean and Dalrymple, 1984); it should be noted that depth effects in this equation will only be significant for $Kh < \pi$.

To simplify the algebra, Eq. (3) can be recast as,

$$\eta_1(r,t) = \int_{-\infty}^\infty \int_{-\infty}^\infty \left\{ \hat{\eta}_1^+(K,t) + \hat{\eta}_1^-(K,t) \right\} e^{i(K.r)} dK, \qquad (6)$$

where "hat" symbols denote the spatial Fourier transforms, with,

$$\hat{\eta}_1^\pm(K,t) = \sqrt{\frac{\Psi(\pm K)}{2}} e^{\mp i(\Omega t)} e^{i\varphi^\pm(K)}. \qquad (7)$$

As indicated above, higher-order wave effects are modeled by including second-order wave components in the ocean surface model. A detailed expression of $\eta_2(r,t)$ is left out due to lack of space.

In the present applications, sea-states are assumed to be fully developed and represented by a Pierson-Moskowitz (PM) directional wave energy density spectrum $\Psi(K_x, K_y)$, parametrized as a function of V_{10}, the wind speed at a 10 m elevation, and with a standard angular spreading function, which is a cosine power s (we use $s = 5$ in the present applications) of direction θ, with respect to the dominant direction of wind waves θ_p. This function is asymmetric, to include a fraction $\xi \in [0,1]$

of the spectral wave energy associated with waves propagating in the direction opposite to the dominant direction (we use $\xi = 0.1$ in the present applications). The corresponding significant wave height is classically obtained as a function of the zero-th moment of the spectral energy density. For instance, for $V_{10} = 10$ m/s, $s = 5$, and $\xi = 0.1$, we find $H_s = 1.71$ m, $L_p = 127.4$ m, and assuming deep water, $T_p = 9.04$ s.

Radar scattering model

Based on Bragg scattering theory, Barrick (1972) first derived expressions for the first- and second-order statistical radar cross-sections, for a monostatic radar configuration; these were later extended to a bistatic configuration (Gill and Walsh, 2001). In monostatic configuration, any radar cell specified on the ocean surface is identified by its range, R, and radar steering angle ϕ_r. The Bragg vector, $\boldsymbol{K}_B$ is defined to point in the radar direction of observation, with a norm equal to $K_B = (2\pi/L_B)$ (see Eq. (1)). In the present radar scattering model, the statistical Doppler spectrum is computed based on a deterministic representation of the complex backscattered signal associated with a given radar cell. For simplicity and due to lack of space, here, we only present first-order terms. Second-order terms, also included in the model, have been found to have little impact on the main findings reported in the paper, and will be discussed later in more detail in an extended paper. The leading contribution to the radar signal is a first-order scattered field, which is proportional to the spatial Fourier transform of η_1 at the Bragg wavenumber vector,

$$S^{(1)}(t) = 4K_B \sum_{\varepsilon=\pm} \hat{\eta}_1^{\varepsilon}(\boldsymbol{K}_B, t) \tag{8}$$

With the exception of a constant coefficient depending on the radar antenna system and the emitted power, the normalized electric signal received by the radar, from each radar cell, is expressed as,

$$V(t) = \mathscr{A} S(t) + \mathscr{N}(t) \quad \text{with} \quad \mathscr{A}(R) = |F(R)|^2 R^{-2} \sqrt{\Delta \mathbb{S}}, \tag{9}$$

a geometric attenuation factor, where $\Delta \mathbb{S} = R \Delta R \Delta \phi_r$, with ΔR and $\Delta \phi_r$ the cells' radial and azimuthal resolutions, respectively; $\mathscr{N}$ is noise, detailed below, and F is the EMW attenuation by the ocean surface, which is computed here using the GRwave model. Assuming an integration time T_i, the radar Doppler spectrum is computed at time t_s as the mean square of the modulus of the Fourier transform of the radar signal, centered on its mean, over time interval $[t_s - T_i/2, t_s + T_i/2]$,

$$I(f_D, t_s) = \frac{1}{T_i} \mid \int_{t_s - \frac{T_i}{2}}^{t_s + \frac{T_i}{2}} V(\tau) e^{2i\pi f_D \tau} d\tau \mid^2, \tag{10}$$

which is easily computed, if the radar signal is calculated/(recorded) at a constant temporal sampling rate $\Delta t = T_i/N$, as a summation from $-N/2$ to $N/2$. Note, in practice, Doppler spectra are computed at a constant time interval $\Delta t_s \leq T_i$, since to better resolve the reconstructed surface currents in time, one assumes some overlap between the time series of radar signal, based on which each Doppler spectrum is computed. The simple expression in Eq. (8) of the first-order backscattered field originates in the classical Rayleigh-Rice theory for the field scattered by a slighly rough surface under a plane wave illumination. It differs from Barrick's standard formulation of HF backscattering, which is expressed in terms of Doppler spectrum and not in the time domain; the Doppler spectrum obtained from Eq. (8), however, coincides with the classical first-order expression. Note, our formulation is a simplification of the more rigorous theory, developed by Walsh and Gill (2000) and Gill and Walsh (2001), for a pulsed dipole source, which takes into account the finite extent of the patch and the finite distance of the source. However, for large radar cells (as compared to the radar wavelength), the expression of the backscattered field from a given surface patch (Eq. 91 in Walsh and Gill (2000)) recovers (up to a constant factor) the expression of the attenuated scattering amplitude in Eq. (9).

Noise model

In the ocean, the backscattered radar signal is affected by thermal noise and various other environmental sources of noise. Since noise is statistically homogeneous and independent of range R, the radar signal attenuation with range makes the Signal to Noise Ratio (SNR) decrease, which limits the effective measuring range of HF radar systems. To simulate environmental noise, besides range attenuation, and the resulting varying SNR with distance, in the simulated radar signal Eq. (9), we add a Gaussian distributed noise, with constant standard deviation σ_N,

$$\mathscr{N}(t) = \sigma_N \{\mathscr{G}_t^R(0, 1) + i\mathscr{G}_t^I(0, 1)\}, \tag{11}$$

where, similar to the signal, noise is a complex number and the subscript t indicates that normally-distributed random values $[\mathscr{G}_t^R(0, 1), \mathscr{G}_t^I(0, 1)]$, with unit standard deviation, are being generated for each time level t.

Diginext field tested Stradivarius in the Golf of Lion area and measured the main Bragg lines' SNR (according to the noise floor) at 200 km during a typical day (wind speed $V_{10} = 10$ m/s); they found an average SNR of 30 dB, with an integration time of 10 min. In the simulations, the value of σ_N (in dB) was adjusted to produce the same SNR at the same distance, as measured, when working with a normalized amplitude $V(t)$. With this constant level of noise in the simulated data, and in view of the attenuation of the radar signal at long distance, the simulated SNR decreases with range in a realistic way, making the underlying surface current gradually less detectable by the HF radar.

ALGORITHMS FOR TSUNAMI DETECTION BY HF RADAR

Based on the shift it causes to the theoretical Bragg frequencies of the HF radar signal, one can reconstruct an ocean surface current from the signal Doppler spectrum, in a series of radar cells and at regular time intervals. The reconstructed currents are projected on directions either radial to the radar for a monostatic deployment or normal to the local radar ellipse for a bistatic deployment. This direct reconstruction, however, can only be achieved where both the radar SNR is sufficiently large and the tsunami current magnitude is sufficiently larger than the background current; simulations of radar scattering for synthetic tsunamis, detailed below (and some more during the conference), will show that the tsunami current magnitude should be at least 0.10-0.15 m/s for an accurate reconstruction to occur. Using Eq. (2) and assuming an incoming tsunami amplitude of $\mid \eta_t \mid = O(0.5)$ m, which is quite large away from nearshore areas, and a minimum current, $\mid \boldsymbol{U}_t \mid \sim 0.2$ m/s, we find the depth range for detection as, $h \leq 61$ m. Hence, direct detection of tsunami currents by way of the HF radar Doppler spectrum appears to be applicable only to detect tsunamis that have already propagated over the continental shelf. Nevertheless, it may be useful for a wide shelf, over which tsunami propagation may still take up to 1 h, as demonstrated in other numerical works and observed for the recent Tohoku 2011 tsunami.

Here, however, we aim at exploiting the property of the Stradivarius radar of being able to measure ocean properties up to 200-300 km, by developing a tsunami detection algorithm that is applicable for tsunami current magnitudes perhaps as low as 0.05 m/s. Such an algorithm would be able to detect an incoming tsunami in much deeper water, beyond the continental shelf, which is much more attractive to be part of a tsunami early warning system; for the above example, the depth for detection would become $h \leq 981$ m, whereas a 1 m incident tsunami would be detectable for $h \leq 3,924$. As pointed out by Lipa et al. (2012), when a tsunami wave train propagates towards the radar, consistent with the succession of crests and troughs (Fig. 1), the current it induces in a given radar cell is oscillatory in time and, for a series of radar cells aligned along a tsunami wave ray, it is also oscillatory in space. Hence, currents reconstructed in two radar cells are highly correlated. Lipa et al. (2012) exploited this property to develop a detection algorithm based

on the spatial correlation of reconstructed currents reaching a specific threshold. However, for their method to work, the tsunami current magnitude must still be sufficiently larger than the background current, and thus this method is limited to shallower water over the shelf.

By contrast, the newly proposed algorithm is based on the observation that, similar to currents, the signals measured/simulated in two radar cells located along the same wave ray, which are modulated by the tsunami current, should also be highly correlated. Moreover, if the radar signal in the deeper water cell is shifted backwards in time by the tsunami propagation time (time lag) along the wave ray from the deeper to the shallower water cell (which is only a function of bathymetry), the correlation of signals should be maximum. In the absence of a tsunami, no change in correlation should occur with time lag, since the random sea states or residual current in the cells are uncorrelated. We will show that this algorithm allows detecting the presence of spatially correlated tsunami currents along a local wave ray, as low as 0.05 m/s, despite significant environmental noise.

In the following, we use both simulated tsunami wave trains and the radar signal simulator to validate the relevance of this algorithm for tsunami detection. For comparison, we also perform the standard reconstruction of currents based on radar Doppler spectra. In both cases, we assess the effect of SNR as a function of range on tsunami detection, for various situations of environmental noise (only selected results are reported here due to lack of space). To simulate the HF radar signal $V(t)$, we apply the scattering model detailed above for a series of radar cells, defined over the ocean area covered by the radar EMWs. In each cell, the center is at a radial distance $\boldsymbol{r}_{mn}$ from the radar (where n denotes the radial range and m the azimuthal range), and sea state is specified by its energy density spectrum $\Psi(\boldsymbol{K})$ (together with normally distributed random values of wave amplitude, $\tilde{a}(\boldsymbol{K})[0,\tilde{\sigma}_{\boldsymbol{K}}]$), as well as a surface current $\boldsymbol{U}(\boldsymbol{r}_{mn}+\boldsymbol{x}_{mn},t)$ (where $\boldsymbol{x}_{mn}$ are coordinates defined at the center of cell (m,n)). This current may contain a background current, in addition to a simulated tsunami current, obtained from separate numerical simulations. The corresponding random surface elevations $\eta(\boldsymbol{r}_{mn}+\boldsymbol{x}_{mn},t)$ are generated in each cell using Eqs. (3) and the backscattered radar signal $V_{mn}(t)$, using Eqs. (8) to (11). Finally, depending on environmental noise level and related SNR, there is a range limitation for practical detection, which is site specific; such environmental noise and range effects are included in the simulations of the radar signal.

Direct tsunami current and elevation reconstruction

In each radar cell, the Doppler spectrum $I_{mn}(f_D,t_s)$ of the radar signal is calculated, at regular time intervals, using Eq. (10) (for an integration time T_i). The primary peaks of the Doppler spectrum, located at frequencies $\pm \mid f_{D_{mn}}^{max}(t_s) \mid$, will be shifted by Δf_B with respect to the theoretical Bragg frequencies $\pm f_B$ proportionally to the current in the cell; hence, the space (over $\boldsymbol{x}_{mn}$ in cell (m,n)) and time (over T_i) averaged surface current $\overline{U}_{r_{mn}}$ can be reconstructed in each cell, along local radial direction $\boldsymbol{r}_{mn}$ and, if the local direction of propagation of the tsunami $\boldsymbol{k}_{t\,mn}$ is known (e.g., based on pre-existing tsunami modeling, Snell's law in the simplest case), Eq. (2) yields the corresponding tsunami elevation, thus,

$$\tilde{\overline{U}}_{r_{mn}}(t_s) = L_B\left(f_{D_{mn}}^{max}(t_s) \pm f_B\right) \;\; ; \;\; \eta_t(\boldsymbol{r}_{mn},t_s) = \frac{\tilde{\overline{U}}_{r_{mn}}(t_s)}{\frac{\boldsymbol{r}_{mn}}{r_{mn}} \cdot \frac{\boldsymbol{k}_{t\,mn}}{k_{t\,mn}}}\sqrt{\frac{h(\boldsymbol{r}_{mn})}{g}} \quad (12)$$

where $h(\boldsymbol{r}_{mn})$ is the depth at the cell center.

Because the reconstructed current also includes the background current, this method only provides good results when the tsunami current is significantly above background. As mentioned before, the Doppler spectrum frequency resolution is $\Delta f_D = 1/T_i$ and thus T_i should be sufficiently large to provide a good resolution, and thus sufficient accuracy for the reconstructed current. Unfortunately, however, the reconstructed current is time-averaged over T_i which, hence, should also be much less than

the tsunami characteristic period T_t. Otherwise, the estimated currents could significantly be underestimated, due to smoothing out by averaging positive and negative values in the tsunami wave train. A practical solution to this problem, assuming long-crested tsunami wave trains in the azimuthal direction (Fig. 1), will be to perform cell-averaging of the Doppler spectra computed for a few cells along the azimuthal direction.
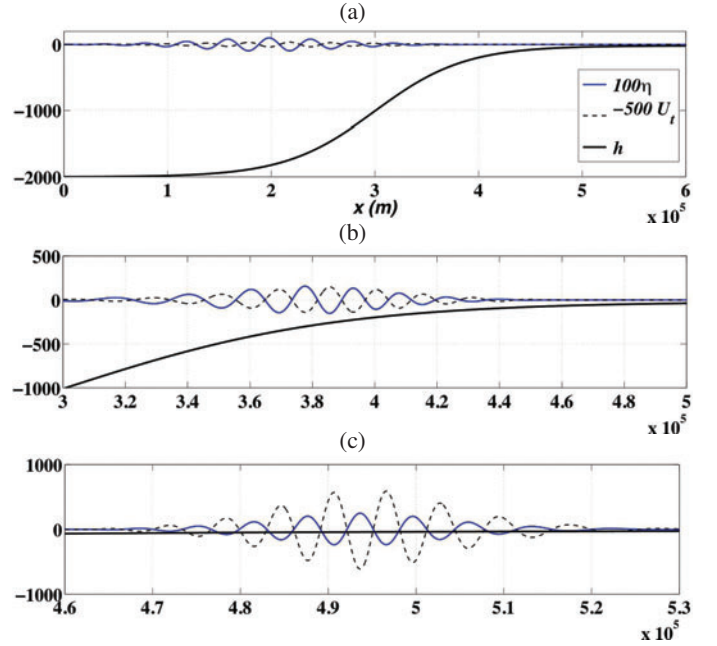

Fig. 3: Idealized "Envelope Soliton" (ES) tsunami wave train propagating over a "tanh" bottom topography, for $A_{t0} = 1$ m, $h_0 = 2,000$ m, $h_1 = 20$ m, $T_t = 300$ s, and $\varepsilon_z = 0.05$, based on the analytical model Eqs. (19) to (20), at times $t =$ (a) 0, (b) 1,895, and (c) 5,670 s. Vertical subplot scale is meter for elevation η and depth h and m/s for current U_t.

Detection algorithm based on signal correlations

To the first-order, along wave rays that can be pre-calculated in a given area, the propagation of tsunami waves, at the long wave celerity $c_t = \sqrt{gh}$, is entirely determined by the bathymetry $h(x,y)$. In the following, we validate the detections algorithms for an idealized tsunami propagating normally onto a shelf and nearshore area that has no longshore variation, i.e., has a depth $h(x)$ (e.g., Fig. 3). In this case, the bathymetric contours are parallel to the straight shore and any tsunami wave train, incident with an angle ϕ_{t0} in deeper water of depth h_0, will refract in a way that is analytically predicted by Snell's law; wave shoaling is also simply predicted by Green's law (see Eq. (2)), corrected by a refraction coefficient obtained from Snell's law (Dean and Dalrymple, 1984). Furthermore, in the simplest possible case of a normally incident tsunami on this bathymetry ($\phi_{t0} = 0$), all wave rays are straight and shore normal, and the refraction coefficient is 1. For linear long waves, the tsunami propagation time between two radar cells, say p and q, centered at r_p in deeper depth $h(r_p)$ and r_q in shallower depth $h(r_q)$, along a radar ray that is normally incident to the bathymetry, is thus given by,

$$\Delta t_{pq} = \int_{r_p}^{r_q} \frac{dr}{\sqrt{gh(r)}} \quad , \text{or} \quad \oint_{s(r_p)}^{s(r_q)} \frac{ds}{\sqrt{gh(s(\boldsymbol{r}))}} \quad (13)$$

for an arbitrary wave ray, where $s(\boldsymbol{r}(x,y))$ denotes the curvilinear abscissa along the ray, with $ds = dx \cos\phi_t + dy \sin\phi_t$.

As discussed above, time series of tsunami current in cells p and q, should be highly correlated when shifted by Δt_{pq}. Thus,

$$\text{corr}\{\overline{U}_{tq}(t - \Delta\tau), \overline{U}_{tp}(t)\} = \frac{1}{T_c}\int_{t-\frac{T_c}{2}}^{t+\frac{T_c}{2}} \overline{U}_{tq}(\tau - \Delta\tau)\overline{U}_{tp}(\tau)d\tau \quad (14)$$

should be maximum, when $\Delta\tau = \Delta t_{pq}$, over a correlation time T_c (which here can be $\gg T_t$) and with the overbar indicating space averaging within each cell. For independent random sea states in each radar cell, the angular frequency changes induced on surface waves by the current, that affect the radar signal by shifting the Bragg frequency, should also be highly correlated when the currents are shifted by their propagation time between cells, and so should be the corresponding radar signals. Hence,

$$\mathrm{corr}\{\mathrm{V}_q(t-\Delta\tau), \mathrm{V}_p(t)\} = | \frac{1}{T_i} \int_t^{t+T_i} \mathrm{V}_q(\tau-\Delta\tau)\mathrm{V}_p^*(\tau)\mathrm{d}\tau | \quad (15)$$

should also be maximum when $\Delta\tau = \Delta t_{pq}$, with V_p and V_q the radar signals in cells p and q, and the star indicating the complex conjugate.

Now, for the background current resulting from both a spatially varying (but nearly stationary at the considered scales) mesoscale current and local effects of environmental conditions (e.g., wind), there should not be any significant correlation between two arbitrarily selected cells, particularly when shifted in time by Δt_{pq}, and hence no influence on Eqs. (14) and (15). Thus, only the spatially coherent surface current caused by the tsunami will affect correlations of the radar signal shifted by the long wave propagation time. This property will be verified in numerical simulations and justifies why a much weaker, but spatially coherent, tsunami current can be detected by this algorithm, even in the presence of a background current of similar or even larger magnitude.

Using this algorithm in a tsunami detection mode (rather than simulation mode), for which the radar signal is continuously measured in a large number of radar cells, a high correlation appearing between radar signals in two cells located along the same wave ray when shifted by the long wave propagation time between those cells, will indicate that a tsunami is approaching the radar. In the range of periods/time scales we are considering, there is indeed no other geophysical phenomenon that can create long wave trains that are spatially coherent, with a current magnitude sufficient to cause measurable Doppler shifts in the HF radar signal. By computing signal correlations in all relevant pairs of cells along a wave ray, one would thus be able to track an incoming tsunami in time, by following the locations of maximum correlation. In the absence of a spatially coherent current, we will see that signal correlations become independent of time lag (i.e., are flat). This difference in correlation pattern around the expected propagation time can be exploited to develop a tsunami detection threshold for this algorithm.

For realistic cases, with a complex, but specified, 2D bathymetry $h(x, y)$, such as the Golf of Lion (Fig. 1), tsunami wave rays can be pre-calculated for a few deep water incidence angles ϕ_{t0}, e.g., corresponding to know tsunami source directions in the far- and near-field, using the "eikonal" equation. One can then identify radar cells along a specific ray and pre-compute expected tsunami propagation times between all pairs of cells (p,q) using the contour integral in Eq. (13).

VALIDATION OF TSUNAMI DETECTION ALGORITHM

Applications of the HF radar detection algorithm to tsunamis in the Golf of Lion will be presented at the conference. Here, we validate the algorithm for an idealized, but realistic enough tsunami wave train for our purpose, over the one-dimensional bathymetry $h(x)$ of Fig. 3, which varies as a hyperbolic tangent from a deeper water h_0 to a shallow shelf h_1. The idealized tsunami wave train is modeled as an incident "Envelope-Soliton" (ES), which we defined as a long-crested train of sinusoidal waves, whose envelope A_t has a solitary wave shape,

$$\eta_t(x,0) = A_t(x,0)\cos\{k_t(x-x_{t0})\} \; ; \; U_t(x,t) = \eta_t(x,t)\sqrt{\frac{g}{h(x)}} \quad (16)$$

$$A_t(x,0) = \frac{A_{t0}}{1-\varepsilon_z}\left\{\mathrm{sech}^2\{\frac{\kappa}{h_{t0}}(x-x_{t0})\} - \varepsilon_z\right\} \; ; \; \kappa = \sqrt{\frac{3A_{t0}}{4h_{t0}}} \quad (17)$$

at time $t = 0$, where $k_t = 2\pi/L_t$ for period T_t, $U_t(x,0)$ is the initial tsunami current from Eq. (2), and the ES peakedness parameter κ is the standard solitary wave value. At time $t = 0$, the ES' middle location is at x_{t0} in depth h_{t0}, maximum amplitude is A_{t0} and wavelength, $L_{t0} = T_t c_{t0}$; the initial ES celerity at its center is, $c_{t0} = \sqrt{gh_{t0}}$ and its wavelength $L_s(0)$ is controlled by the truncation parameter, $\varepsilon_z \ll 1$, such that,

$$| \eta_t(\pm\frac{L_s}{2},0) | = 0 \quad \text{with} \quad L_s(0) = \frac{2h_{t0}}{\kappa}C_z \; , \; C_z = \mathrm{acosh}\sqrt{\varepsilon_z^{-1}} \quad (18)$$

The ES is initially defined by a set of points $x_i(0)$ $(i = 1,...)$, spaced out by Δx over the free surface. For later times t, these points propagate with the local celerity $c_{t_i}(h_i)$ while local elevations η_i change based on Green's law (Eq. (2)). These properties allow us defining a set of linearized equations to iteratively propagate the ES wave train over the specified bathymetry, from time t to $t + \Delta t$ (with Δt a small time step) as,

$$x_i'(t+\Delta t) = x_i(t) + c_{t_i}\Delta t \quad \text{with,} \quad c_{t_i} = \sqrt{gh(x_i(t))} \quad (19)$$

$$\eta_{t_i}'(x_i'(t+\Delta t)) = \eta_{t_i}(x_i(t))\left\{\frac{h(x_i(t))}{h(x_i'(t+\Delta t))}\right\}^{\frac{1}{4}} \quad (20)$$

At a given time t, once the ES has propagated to locations x_i' with elevations $\eta_{t_i}'(x_i')$, the latter are reinterpolated over the initial grid points and the ES wave train is truncated by applying Eq. (18). Finally, the tsunami horizontal current $U_t(x_i(t+\Delta t))$ is computed using Eq. (16). This process is repeated for the next time step, and so forth.

In the following, we present results for the ES tsunami case shown in Fig. 3, with $A_{t0} = 1$ m and $T_t = 300$ s; bathymetry varies between $h_0 = 2,000$ m and $h_1 = 20$ m on the continental shelf; the ES is truncated using $\varepsilon_z = 0.05$ and specified as far left as possible in the domain; the initial location of its maximum is at, $x_{t0} = 197.93$ km in depth $h_{t0} = 1,829$ m ($\kappa = 0.0202$), with a maximum current $U_t^{max}(x_{t0}, 0) = 0.07$ m/s.

Before testing the algorithm, we validated the simplified ES propagation Eqs. (19) and (20) by comparing to a numerically exact (but more computationally demanding) solution of the fully nonlinear potential flow problem, using a Boundary Element Method (BEM; Grilli and Subramanya (1996)). The computational domain spans from $x = 0$ to 600 km. A fine $\Delta x = 30$ m spatial mesh and constant time step $\Delta t = 5$ s are used in the analytical solution but, to reduce computational effort, the BEM boundary is only discretized with 1212 nodes and 1004 cubic elements, with time step $\Delta t \simeq 2.4$ s (dynamically adjusted as depth reduces).
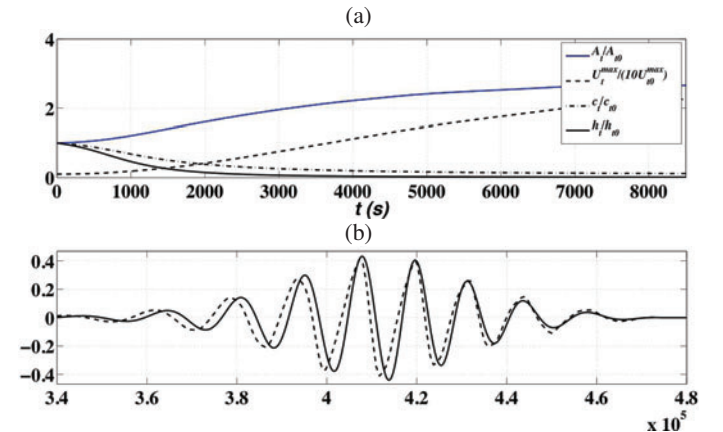

Fig. 4: Case of Fig. 3: (a) key parameters of ES tsunami calculated with the analytical model as a function of time; (b) comparison of analytical solution (solid), with BEM solution (dash), for horizontal current value $U_t(x,t)$ (m/s) at $t = 2,234$ s (on the free surface in the BEM model).
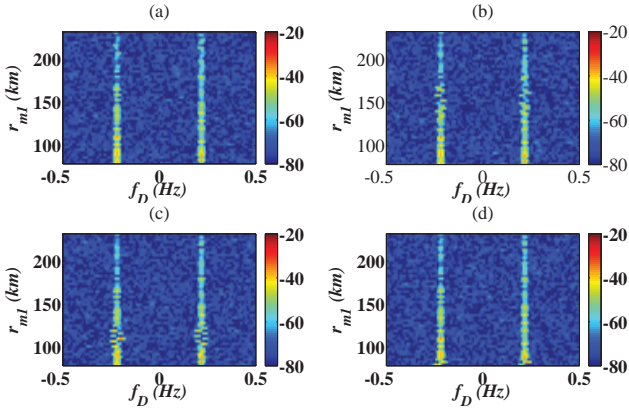
Fig. 5: First-order Doppler spectra (color scale in Db) from HF radar simulator applied to ES tsunami propagation (Fig. 3), for 51 cells at $r_{m1} = 80$ to 230 km from the radar (with $\phi_{r_1} = -90$ deg.), after: (a) 30, (b) 60, (c) 90, et (d) 120 min.
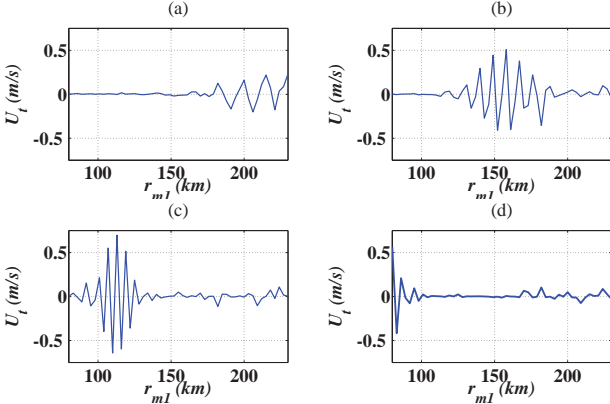

Fig. 6: Reconstructed ES currents from Doppler spectra of Fig. 5.

Both the initial elevation and horizontal current of this idealized ES tsunami are shown in Fig. 3a. The analytical model is applied first, to propagate the ES tsunami until its front reaches $x = 600$ km, which occurs at $t = 10,800$ s (3 h). Instantaneous values of free surface elevation and current are shown in Figs. 3b,c, at $t = 1,895$ and 5,670 s, respectively. At these times, the ES maximum is at $x_t = [377,640, 493,650]$ m, in depth $h_t = [302.48, 40.73]$ m, with a maximum amplitude $A_t = [1.57, 2.49]$ m, and current $U_t^{max} = [0.28, 1.22]$ m/s. As depth decreases, there is a gradual increase of both elevation and current, while the dominant wavelength L_t decreases, as a result of decreasing phase velocity c_t; hence, the tsunami wave train becomes gradually shorter. Key parameters of the ES are plotted as a function of time in Fig. 4a. To limit the BEM computational effort, the validation was limited to $t \leq 2,234$ s, which corresponds to the ES maximum arriving at $x_t = 408$ km in depth $h_t = 170.4$ m. Fig. 4b compares horizontal current $U_t(x,t)$ computed with the analytical model and the BEM (on the free surface) and shows a reasonable agreement, with only a slightly larger value of the dominant wavelength and slightly lower current value in the BEM solution. This can be explained by the nonlinear amplitude dispersion effects in the latter, which mitigate the decrease of tsunami phase speed with depth. Nevertheless, it can be concluded from this comparison that the analytical model is sufficiently accurate to simulate the ES tsunami propagation and transformations over the specified bathymetry, for the purpose of validating the tsunami detection algorithms by HF radar. The faster analytical model will allow rapidly obtaining simulated data sets of tsunami elevation and current for simulating the HF radar signal in selected radar cells located at $|r_{m1}| = x_m$ $(m = 1, ..., M)$. The model will also allow computing the spatially averaged surface current in each cell $\overline{U}_{tm}(t)$, as a function of time, as well as the current memory term in Eq. (4).

Application of HF radar simulator to ES tsunami data

Assuming for simplicity, a monostatic radar configuration (or a large enough range for the signal to become nearly monostatic), the signal is being simulated in a series of cells located in radial directions r_{mn} of azimuth ϕ_{r_n} measured from x $(m = 1, ..., M; n = 1, ..., N)$, for a radar located at $(0,0)$. The radar signal is modulated by the tsunami current projected on these radial directions (assuming to start with that there is no residual current, $U_r = 0$),

$$U_{tR}(t, r_{mn}) = U_t(t, x_{mn}, y_{mn}) \cdot r_{mn} \quad ; \quad r_{mn} = x_{mn}e_x + y_{mn}e_y \quad (21)$$

with, (e_x, e_y) the unit vectors in the x- and y-directions.

We only present results for first-order waves η_1 and backscattered signal $S^{(1)}$, assuming the characteristics of the 4.5 MHz Stradivarius radar. Second-order effects do not change the main findings and will be discussed at the conference. Environmental noise and range decay are simulated by adding $\mathcal{N}_{mn}(t)$ to the signal $\mathcal{A} S_{mn}(t)$ computed in each cell, based on Eqs. (11) and (9). For the idealized ES tsunami (Fig. 3), we use a single azimuth direction, $\phi_{r_1} = 180$ deg. $(n = 1;$ i.e, looking directly away and normal to shore), with an angular spacing $\Delta\phi_r = 6$ deg.; hence, $U_{tR}(t, r_{m1}) = -U_t(t, x_m)$. The radar signal is computed for 7,200 s in cells spaced out by $\Delta r = 3$ km, at a distance, $r_{m1} = -x_m = 80$ to 230 km from the radar (corresponding to depths between 30.5 and 348.5 m). In each cell, the random sea state is spatially discretized with $\Delta x = \Delta y = 3$ m, assuming the PM energy spectrum Ψ_{PM} with $V_{10} = 10$ m/s discussed above, with $\theta_p = 0$ deg. Wavenumber vectors, $K = (K_x, K_y)$, vary within $[-K_{max}, K_{max}]$ by steps $\Delta K = 2\pi/1000$, with $K_{max} = 2\pi/(2\Delta x)$, which yields 333 x 333 wavenumbers. Waves are modulated by the ES tsunami current modeled in the previous section.

We first perform a standard reconstruction of currents based on HF radar Doppler spectra, computed with Eq. (10) for $T_i = 120$ s $(< T_t/2)$, over a frequency range $[-f_{Dmax}, f_{Dmax}]$, with here, $f_{Dmax} = 0.5 = 2.3f_B$ Hz. (integration intervals are $[t_s - 0.67T_i, t_s + 0.33T_i]$; new spectra are computed with a $0.33T_i = 40$ s time step). Doppler spectra are shown in Fig. 5, as a function of range r_m, after 30, 60, 90 et 120 min. of propagation and shoaling of the ES tsunami; as expected, there are two maxima in each spectrum at the theoretical Bragg frequencies ± 0.216 Hz. [Because of the asymmetric and directional PM spectrum, the two maxima have different magnitudes.] Outside of the neighborhood of the Bragg frequencies, the spectral intensity rapidly decreases to the level of the environmental noise. The ES tsunami current causes an oscillatory shift of the spectrum maxima around the Doppler frequencies, which mimics wave shoaling and refraction. As range increases, however, the strength of the spectrum maxima rapidly decreases, down to the noise level, and hence the oscillations induced by the current become gradually less detectable.

Fig. 6 shows the reconstructed mean currents based on Doppler spectra in Fig. 5. For short ranges, one recovers well both the expected current magnitude and variability, as the ES tsunami propagates towards shallower depth. Despite the environmental noise and the fairly large depth in the most distant cells, currents can still be fairly accurately inverted by this method, as can be seen by comparing, e.g., Fig. 6b with Fig. 4b. This is because for this strong tsunami case, maximum currents even at 200 km from the radar are still on the order of 0.15 m/s. Other cases for more moderate tsunamis (which will be presented at the conference), however, will show that tsunami currents need to be at least 0.15 m/s to be detected by this method, for typical environmental noise levels.

We now apply the detection algorithm to the same case, by computing correlations of the radar signal between cells using Eq. (15), with $T_c = 300$ s. Fig. 7a shows the correlations computed between pairs of cells 1 and $p = 2, ...51$, shifted by the travel time to cell 1, $\Delta t_{1p} = 176 - 5,337$ s, as a function of an additional time lag. We see elevated correlations for lags [-50, 50] s to a 160 km range and [-50, 150] s beyond that.
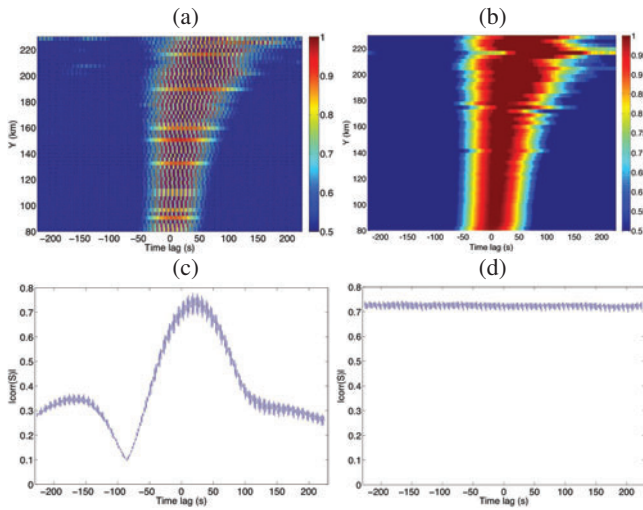
Fig. 7: Test of detection algorithm for ES case of Fig. 3: (a) Signal correlation (color scale) between cells 1 and $p = 2, ...51$ (Eq. (15)), shifted by travel time to cell 1, $\Delta t_{1p} = 176 - 5,337$ s, as a function of an additional time lag; (b) Same as (a) for the *analytical* signals; (c) Mean correlation over all pairs of cells; (d) Same as (c) without the surface current.

Outside of these intervals, correlations quickly become negligible. In Fig. 7c, we see a strong peak of the mean correlation over all pairs of cells near lag zero; Fig. 7d shows that there is no trend in correlation with time lag, for the same case without the surface current. These results confirm the relevance of the proposed detection algorithm. Fig. 7b finally shows that even better results, with higher correlations, near one, can be obtained by eliminating high-frequency oscillations in correlation, using the *analytical* signals instead (the latter are easily obtained for simulated or measured signals by applying a Fourier transform (FT) to the signal, removing the negative frequency values, and applying an inverse FT).

Similar results can be obtained when using both second-order waves and radar signals. A sensitivity analysis was done to parameters that weaken the radar signal (or decrease its SNR), i.e. : (i) an increasing environmental noise (including residual current); (ii) a decreasing wind speed; or (iii) a decreasing tsunami amplitude. Although the maximum range for detection slightly decreases, we found that a peak of correlation still occurs in a detectable manner near lag zero, while no trend in correlation occurs in the absence of a surface current. By contrast, for a weaker SNR, the direct detection of currents by inverting Doppler spectra stops working, except at short ranges, in shallow water where currents are stronger. Details of these cases will be shown during the conference.

CONCLUSION

Although applied to an idealized tsunami and bathymetry, present results indicate that the effects on radar signal correlations of tsunami currents as low as 0.05 m/s can be detected with our proposed new HF radar detection algorithm; hence, this allows tsunami detection beyond the shelf. In many situations, actual tsunamis behave as our idealized case. For instance, in an area with a wide shelf such as the Gulf of Lion in Southern France (Fig. 1), which has a nearly 2D plane beach topography in most of its mid-section facing Camargue, owing to refraction, all tsunamis, whichever their initial incidence in deeper water, end up propagating over the shelf as a series of long-crested waves, nearly parallel to the bathymetric contours. With minor changes to the approach presented below, one can consider tsunamis that are approaching from a direction ϕ_{t0} over the same idealized bathymetry, by applying Snell's law. Solving the eikonal equation for an arbitrary bathymetry, actual

case studies can be solved. Details and more results will be given at the conference.

REFERENCES

Barrick, D. (1972). First-order theory and analysis of MF/HF/VHF scatter from the sea. *IEEE Transactions on Antennas and Propagation*, 20(1):2–10.

Barrick, D. and Weber, B. (1977). On the nonlinear theory for gravity waves on the ocean's surface. Part II: Interpretation and applications. *Journal of Physical Oceanography*, 7(1):11–21.

Barrick, D. E. (1979). A coastal radar system for tsunami warning. *Remote Sensing of Environment*, 8(4):353–358.

Dean, R. G. and Dalrymple, R. A. (1984). *Water Wave Mechanics for Engineers and Scientists*. Prentice-Hall.

Dzvonkovskaya, A. (2012). Ocean surface current measurements using HF radar during the 2011 Japan tsunami hitting Chilean coast. In *Geoscience and Remote Sensing Symp. (IGARSS), 2012 IEEE Intl.*, pages 7605–7608. IEEE.

Dzvonkovskaya, A., Gurgel, K.-W., Pohlmann, T., Schlick, T., and Xu, J. (2009). Simulation of tsunami signatures in ocean surface current maps measured by HF radar. In *OCEANS 2009-EUROPE*, pages 1–6. IEEE.

Gill, E. and Walsh, J. (2001). High-frequency bistatic cross sections of the ocean surface. *Radio Science*, 36(6):1459–1475.

Grilli, S. T., Harris, J. C., Tajalli-Bakhsh, T., Masterlark, T. L., Kyriakopoulos, C., Kirby, J. T., and Shi, F. (2013). Numerical simulation of the 2011 Tohoku tsunami based on a new transient FEM co-seismic source: Comparison to far- and near-field observations. *Pure and Applied Geophysics*, 170:1333–1359.

Grilli, S. T., Ioualalen, M., Asavanant, J., Shi, F., Kirby, J. T., and Watts, P. (2007). Source constraints and model simulation of the December 26, 2004 Indian Ocean tsunami. *J. Waterw. Port Coastal and Oc. Eng.*, 133(6):414–428.

Grilli, S. T., O'Reilly, C., Harris, J. C., Tajalli-Bakhsh, T., Tehranirad, B., Banihashemi, S., Kirby, J. T., Baxter, C. D., Eggeling, T., Ma, G., and Shi, F. (2015). Modeling of SMF tsunami hazard along the upper US East Coast: Detailed impact around Ocean City, MD. *Natural Hazards*, 76:705–746.

Grilli, S. T. and Subramanya, R. (1996). Numerical modeling of wave breaking induced by fixed or moving boundaries. *Comput. Mech.*, 17(6):374–391.

Grilli, S. T., Taylor, O.-D. S., Baxter, C. D., and Maretzki, S. (2009). Probabilistic approach for determining submarine landslide tsunami hazard along the upper East Coast of the United States. *Marine Geology*, 264(1-2):74–97.

Grilli, S. T. and Watts, P. (2005). Tsunami generation by submarine mass failure Part I : Modeling, experimental validation, and sensitivity analysis. *Journal of Waterway Port Coastal and Ocean Engineering*, 131(6):283–297.

Gurgel, K.-W., Dzvonkovskaya, A., Pohlmann, T., Schlick, T., and Gill, E. (2011). Simulation and detection of tsunami signatures in ocean surface currents measured by HF radar. *Ocean Dynamics*, 61(10):1495–1507.

Heron, M., Prytz, A., Heron, S., Helzel, T., Schlick, T., Greenslade, D., Schulz, E., and Skirving, W. (2008). Tsunami observations by coastal ocean radar. *International Journal of Remote Sensing*, 29(21):6347–6359.

Hinata, H., Fujii, S., Furukawa, K., Kataoka, T., Miyata, M., Kobayashi, T., Mizutani, M., Kokai, T., and Kanatsu, N. (2011). Propagating tsunami wave and subsequent resonant response signals detected by HF radar in the Kii Channel, Japan. *Estuarine, Coastal and Shelf Science*, 95(1):268–273.

Ioualalen, M., Asavanant, J., Kaewbanjak, N., Grilli, S. T., Kirby, J. T., and Watts, P. (2007). Modeling the 26th December 2004 Indian Ocean tsunami: Case study of impact in Thailand. *J. Geophys. Res.*, 112:C07024.

Lipa, B., Barrick, D., Saitoh, S.-I., Ishikawa, Y., Awaji, T., Largier, J., and Garfield, N. (2011). Japan tsunami current flows observed by HF radars on two continents. *Remote Sensing*, 3(8):1663–1679.

Lipa, B., Isaacson, J., Nyden, B., and Barrick, D. (2012). Tsunami arrival detection with high frequency (HF) radar. *Remote Sensing*, 4(5):1448–1461.

Lipa, B. J., Barrick, D. E., Bourg, J., and Nyden, B. B. (2006). HF radar detection of tsunamis. *Journal of Oceanography*, 62(5):705–716.

Tappin, D. R., Grilli, S. T., Harris, J. C., Geller, R. J., Masterlark, T., Kirby, J. T., Shi, F., Ma, G., Thingbaijamg, K., and Maig, P. (2014). Did a submarine landslide contribute to the 2011 Tohoku tsunami ? *Mar. Geol.*, 357:344–361.

Tappin, D. R., Watts, P., and Grilli, S. T. (2008). The Papua New Guinea tsunami of 1998: anatomy of a catastrophic event. *Natural Hazards and Earth System Sciences*, 8:243–266.

Walsh, J. and Gill, E. (2000). An analysis of the scattering of high-frequency electromagnetic radiation from rough surfaces with application to pulse radar operating in backscatter mode. *Radio Science*, 35(6):1337–1359.

Weber, B. and Barrick, D. (1977). On the nonlinear theory for gravity waves on the ocean's surface. Part I: Derivations. *Journal of Physical Oceanography*, 7(1):3–10.